Flexible and lightweight graphene grown by rapid thermal processing chemical vapor deposition for thermal management in consumer electronics

Satendra Kumar[1,2], Manoj Goswami[1,2], Netrapal Singh[1,2], Uday Deshpande[3], Surender Kumar[1,2,*], N. Sathish[1,2,*]

（1. *Academy of Scientific and Innovative Research (AcSIR)*, *Ghaziabad* 201002, *India*;
2. *CSIR - Advanced Materials and Processes Research Institute (AMPRI)*, *Bhopal* 462026, *India*;
3. *UGC-DAE Consortium for Scientific Research*, *University Campus*, *Indore* 452001, *India*）

Abstract： Next-generation consumer electronics require excellent thermal management. Graphene is a good choice because its thermal conductivity is 13 times that of copper. Single-, bi- and few-layer graphene (SLG, BLG, FLG) with large sp^2 domains were grown by rapid thermal processing chemical vapor deposition (RTP-CVD) from CH_4 and H_2 using Ar as the diluting gas. The quality of graphene was investigated by Raman spectroscopy and TEM. To demonstrate the heat dissipation capability of RTP-CVD-grown graphene, a 2 TB solid state drive was used and the temperature was measured by a FLIR thermal camera. Results indicate that high thermal conductivity graphene was prepared by diluting the precursor gas with Ar. SLG was prepared at a growth temperature of 1 000 °C and a time of 25 min. A transition from FLG to high-quality BLG was observed at low H_2 concentrations. Using SLG, there was a 5 °C lower temperature rise than using a commercial copper heat dissipator. The heat dissipation ability of SLG was approximately 200 times that of commercial copper heat dissipators.

Key words: Graphene; Thermal management; Consumer electronics; Chemical vapour deposition

1 Introduction

Innovation in thermal management technologies is driven by the continual downsizing and rising power density of electronic devices. Due to their hefty mass, such as metal heat sinks, conventional heat removal solutions, can not satisfy the needs of portable electronic devices[1–3]. In the realm of electronic packaging, composites of a metal matrix with excellent thermal conductivity and adjustable coefficients of thermal expansion have attracted particular interest. Due to its excellent thermal conductivity, copper is widely used to spread heat in electronic devices[4]. Because of its exceptional thermal conductivity (5 300 W/mK), high flexibility, and lightweight, graphene has been regarded as a superior thermal interface material[5–7]. Rapid phonon group velocity (23.6 m/s for LA branch) and a lengthy phonon mean free path (240 nm) combine to give graphene its extremely high thermal conductivity[8]. The thermal conductivity of graphene is decreased by defects including vacancies, isotopic doping, and chemical functional groups. Several ways of graphene synthesis methods have been reported such as chemical and electrochemical exfoliation[9], epitaxial growth on the SiC crystal[10], and growth through CVD[11]. Chemically synthesized graphene oxide (GO) has been used to prepare metal composite for heat dissipation. It enhances the thermal conductivity (260 W/mK or 15%) of Aluminum but not up to the mark[12]. Because chemically synthesized graphene has several defects and remaining functional groups which reduce the thermal conductivity. Chae et al. reported enhanced heat dissipation by healing the defects in reduced-GO[13]. In comparison to the thermal conductivity of GO (1.92 W/mK), the thermal conductivity of reduced-GO was increased to 9.90 W/mK. Additionally, the defect-healed reduced-

Received date: 2022-12-17; **Revised date:** 2023-01-30

Corresponding author: N. Sathish. E-mail: sathishrn@gmail.com;
Surender Kumar. E-mail: surender@ampri.res.in

Author introduction: Satendra Kumar. E-mail: satendra12791@gmail.com

Supplementary data associated with this article can be found in the online version.

GO was successfully used as a heat-dissipating material, causing it to cool down swiftly by 36 °C. Rho et al. demonstrated porous copper/SLG/reduced-GO composite for a fanless heat dissipator[14]. With a 9 °C lower peak temperature, the porous copper/SLG/reduced-GO composite dissipated heat more quickly than copper.

However, CVD-grown graphene with a large area, defects-free, and self-limiting to a single or few layers, is very suitable for mass production with easily transferrable[15]. RTP-CVD is different from conventional CVD due to rapid thermal ramping and cooling. The conventional CVD setups require high temperatures to grow either semiconductor or 2D materials such as graphene. On the other hand, RTP-CVD requires comparatively low temperatures with fast ramping and cooling up to 15 °C/s. To obtain defects-free and high-quality graphene through RTP-CVD, still there is a requirement to optimize various parameters like growth temperature, time, chamber atmosphere, precursor gases and substrates[16]. Raman spectroscopy is a promising technique for the investigation of graphene quality[17–18]. Raman spectroscopy along with high-resolution TEM can distinguish the number of layers, defect, and doping level in graphene[19–20].

Herein, we have reported the effect of growth parameters in RTP-CVD to engineer the defects in graphene. With a one-step growth parameter, graphene sheets were investigated by Raman spectroscopy and high-resolution TEM. The high-quality graphene is demonstrated as a flexible and lightweight heat dissipator for consumer electronics.

2 Experimental section

2.1 Growth of graphene

An RTP-CVD (APT-TF200) based bottom-up approach is used to grow graphene recipes on a 25 μm thick copper foil. Initially, the copper foil was annealed under H_2 at 100 standard cubic centimeters per minute (mL/min) for 30 min. During the growth of 10 min, the precursor (CH_4 and H_2) ratio of 12 : 4 mL/min was maintained, with chamber pressure in the range of 2.5-4.0 Mbar. The substrate temperature was maintained at 1 000 °C throughout the annealing and growth processes. Ar concentration was varied for H_2 dilution. The sample designation for 70, 80 and 100 mL/min of Ar concentration is Ar-70, Ar-80 and Ar-100, respectively. Pristine SLG is prepared at growth temperature and time of 1 000 °C and 25 min, respectively. Graphene transfer on the copper grid for the TEM study was done with a wet chemical method as shown schematically in Fig. 1 and is explained in the supplementary information (SI) section.

2.2 Growth mechanism of graphene

For the removal of the native oxide layer and smoothening of the copper surface, a 30 min annealing was done in the presence of molecular H_2 (100 mL min^{-1}). Due to annealing, some H_2 is diffused inside the copper foil. This atomic H_2, impurity oxides, defects, and grain boundaries over/inside the copper foil are the basic building blocks for graphene nucleation on Cu (111)[21]. Due to the catalytic decomposition of CH_4 over the surface of the copper possible dimers, trimers, and adatoms are generated as equations (1) & (2) and schematically shown in Fig. 2(a):

$$CH_4(g) \rightarrow CH_4(s) \quad (1)$$

$$CH_x(s) + (s) \rightarrow CH_{x-1}(s) + H(s) \quad (2)$$

The equation (2) continues until the whole CH_x is converted into C(s) and H(s)[22–23]. A large concentration of H_2 blocks the graphene nucleation sites on copper foil. Because of that, at a lower argon amount (Ar-70), a large number of point-defected graphene sheets were grown. The increment of argon concentration (dilution of H_2) is responsible for the activation of large catalytic site(s) on copper to grow high-quality and defects-free BLG and SLG. For Ar-100, graphene growth continues to form large four-armed dendritic structures and tries to cover a large portion of the copper foil. As the chamber is more diluted with H_2 gas, the precursor is also getting diluted which leads to the termination of graphene growth. The general equation (3) of graphene growth can be written as:

$$\text{Graphene} + C_xH_y(s) \Leftrightarrow (\text{Graphene} - C_x) + yH(s) \quad (3)$$

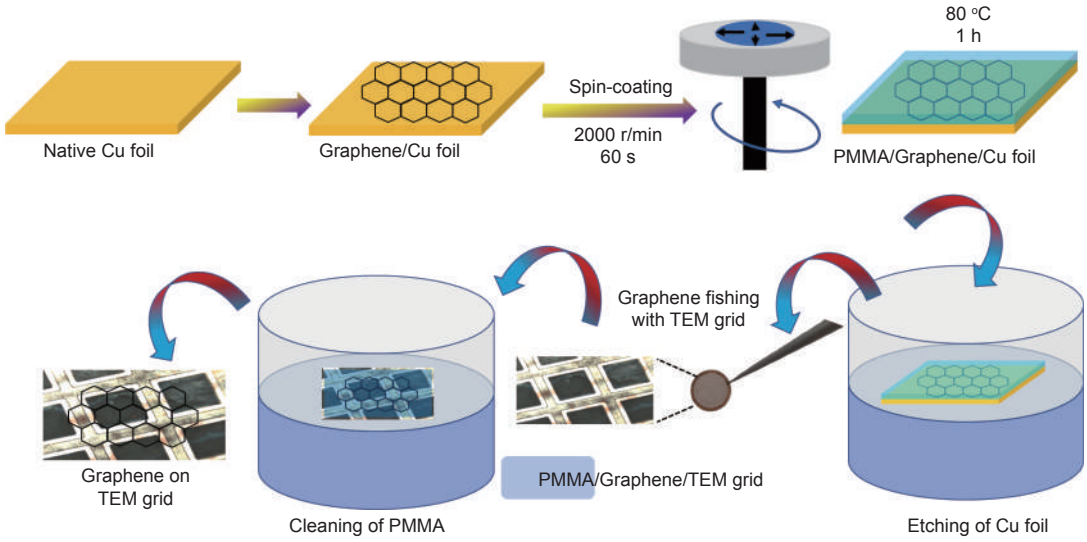

Fig. 1 Schematic representation of graphene transfer on TEM Cu grid

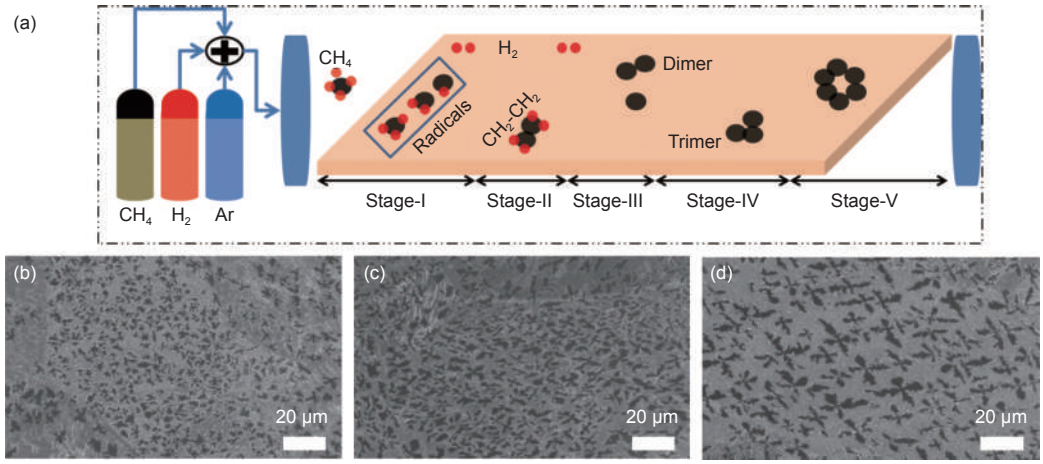

Fig. 2 (a) The schematic representation of chemisorption/deposition of graphene on copper foil. Stage-I: dissociative dehydrogenation of CH_4, Stage-II: dimerization, Stage-III & Stage-IV: trimerization and migration, and Stage-V: growth of graphene. FE-SEM images of (b) Ar-70, (c) Ar-80 and (d) Ar-100 samples

It means pristine SLG require more growth time to cover the whole substrate. Inspired by the above discussions, SLG is also grown only by increasing growth time to 25 min (discussed later).

3 Results and discussion

Field-emission scanning electron microscopy (FE-SEM) images in Fig. 2(b-d) show a close relationship between the number of nuclei per unit area and the percentage area covered with H_2 dilution (increasing Ar concentration). Randomly shaped graphene flakes to four-armed large dendritic flakes are grown by H_2 dilution. The copper surface is etched properly upon H_2 dilution which results in large crystallite and defects-free BLG. For Ar-100, dendritic flakes are very organized and grown in a matrix fashion. Fig. S1 shows that the number of nuclei per unit area falls drastically from 3 200 (Ar-70) to 2 000 (Ar-100) in a concave-down fashion. At low Ar flow, the copper surface was not etched and smoothed properly due to which more nucleation sites were garnered which results in defective FLG (Ar-70 and Ar-80).

Raman spectroscopy is used to confirm the graphene growth, quality, and etching of the native oxide layer. A full-range Raman spectrum of Ar-100 sample in the range of 1 100-3 000 cm^{-1} is provided in Fig. S2. Here, it is very clear that there is no such *D*-peak observed that corresponds to structural defects in RTP-CVD graphene sheets. On the other hand, a weak

peak at 2 450 cm^{-1} is attributed to both a *D* phonon and acoustic longitudinal phonon (*D*"), hence the combination is denoted by the notation *G**-band. Stacked Raman spectra of as-grown graphene are shown in Fig. 3(a). With the absence of defect band (ω_D), graphitic (ω_G) and double resonance signature (ω_{2D}) are obtained in each case. The graphene quality is monitored with I_{2D}/I_G ratio, and FLG to BLG quality is improved upon the H_2 dilution. The large full width at half maxima (FWHM) is found for the sample Ar-70 (23 and 61 cm^{-1} for ω_G and ω_{2D}) due to improper etching and defects (Fig. 3(b, c)). The *G*- and 2*D*-peaks are deconvoluted with one (at 1 607 cm^{-1}) and two (2 659 and 2 720 cm^{-1}) sub-peaks, respectively. The improper etching and native copper oxides are also monitored in different locations of Ar-70 (Fig. 3(d)). Four different native oxide peaks of CuO (at 215 and 632 cm^{-1}) and Cu_2O (at 148 and 412 cm^{-1}) are found which resulted in a defective and small domain FLG[24]. As the H_2 concentration was diluted more (Ar-80 and Ar-100), *G*-peak is blue-shifted with narrow FWHM while 2*D*-peak shifted to the pristine BLG's position, shown in Fig. 3(e-h). The 2*D*-peak of Ar-100 is further deconvoluted with four Lorentzian peaks (2 673, 2 685, 2 693 and 2 714 cm^{-1}) which is the strong signature of BLG.

The graphene qualities mentioned above are also confirmed with Raman mapping which gives a clear picture. A 20.50 μm × 20.50 μm area was selected for the mapping of each sample. Fig. 4(a, d, g) represents the ω_G mapping of Ar-70, Ar-80 and Ar-100, respectively. The ω_G of Ar-70 (~ 1 590 cm^{-1}) and Ar-80 (~ 1 590 cm^{-1}) is somewhat red-shifted (green region: low wavenumber) from the nanocrystalline graphene position ~ 1 600 cm^{-1}. The red-shifting of ω_G in Ar-70 and Ar-80 is due to tension that can be seen in the FWHM mapping in Fig. S3(a, e). Since *G*-peak is under tension due to the distorted honeycomb structure, which leads to the widening of Raman spectra of the 2*D* band in Fig. S3(b, f). The CuO is also mapped around 632 cm^{-1} in Fig. S3(c). Fig. S3(d) shows clear picture of CuO intensity variation. The ω_{2D} mapping of Ar-70, Ar-80 and Ar-100 can be seen in Fig. 4(b, e, h). However, in the mapping of ω_{2D}, most of the region is red-shifted in Ar-70. The further dilution of H_2 leads to the blue-shifting of the 2*D*-band in the case of Ar-80 and Ar-100. Almost every dendrite of graphene is covered with nanocrystalline BLG in Ar-100 and narrow FWHM from 40-80 cm^{-1} in Fig. S3 (h). The above behaviour more clearly can be seen in Fig. S4 (a, b, d, e, g, h), zoomed area (red circles) of particular interest in Fig. 4. Fig. 4 (c, f, i) represents the qual-

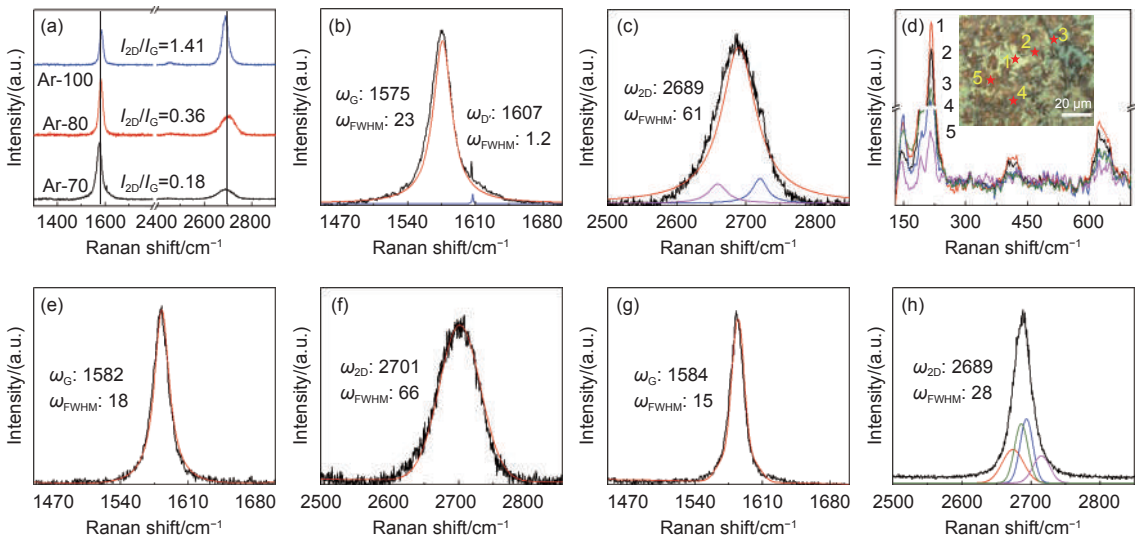

Fig. 3　(a) Stacked Raman spectra of Ar-70, Ar-80 and Ar-100 with the I_{2D}/I_G ratio. (b, c, d) *G*-band (ω_G), 2*D*-band (ω_{2D}), and native oxide Raman spectra for Ar-70. (e, g) and (f, h) is the *G*- and 2*D*-band spectra for Ar-80 and Ar-100, respectively. The G-band position, 2*D*-band position, and FWHM (ω_{FWHM}) are in cm^{-1}

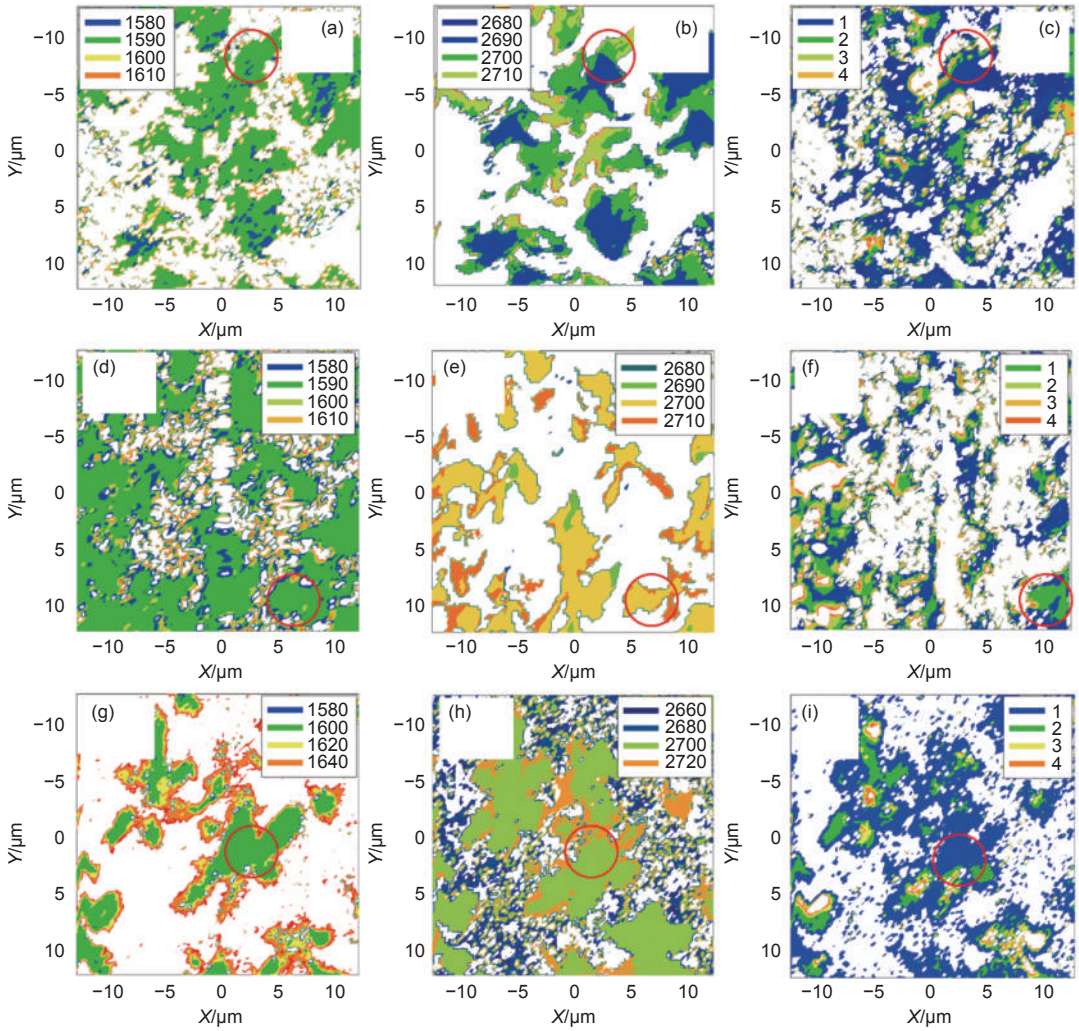

Fig. 4 Two-dimensional plots of Raman mapping of (a, d, g) *G*-band, (b, e, h) 2*D*-band, and (c, f, i) I_{2D}/I_G ratio for Ar-70, Ar-80 and Ar-100, respectively

ity distribution (I_{2D}/I_G ratio) of as-grown graphene for Ar-70, Ar-80 and Ar-100, respectively. This discussion is clearer in Fig. S4 (c, f, i) for Ar-70, Ar-80 and Ar-100, respectively. The central region of two-dimensional images is mostly covered with respective graphene layers but the edges have I_{2D}/I_G ratio greater than 4 which may lead to the turbostraticity which will be discussed later.

Vacancy defects, edges, linear chains, bond rotations, and layer numbers are investigated by high-resolution TEM for a better understanding of as-prepared graphene. High-resolution TEM images of the Ar-70 sample are shown in Fig. 5(a, b) and a range of point defects are present. The mono- and multi-vacancies are directly observable including an extended zigzag monovacancies chain (blue highlight). A schematic representation of point defects is shown in Fig. 5 (c). Fig. S5(a-c) shows different types of defects such as point, line and vacancy defects in Ar-70. FLG edges are shown in Fig. S5 (d, e) between the dashed yellow lines. The sextet of the SAED pattern has a different brightness and shows a non-AB-stacked graphene layer having a range of twist angles, shown in Fig. 5 (d). As H_2 is diluted (Ar-80), the etching of copper foil was enhanced which leads to the AB-stacked (Bernal Stacking) FLG with layer numbers and fewer defects, shown in Fig. 5(e-g). The SAED pattern in Fig. 5(h) shows an AB-stacked FLG with rotational angles between 2° and 40°. The layer numbers are reduced from ~ 10 (Ar-70) to 6 (Ar-80) due to the proper etching. Further dilution of H_2 (Ar-100) produces BLG with lesser defects, shown in Fig. 5(i,

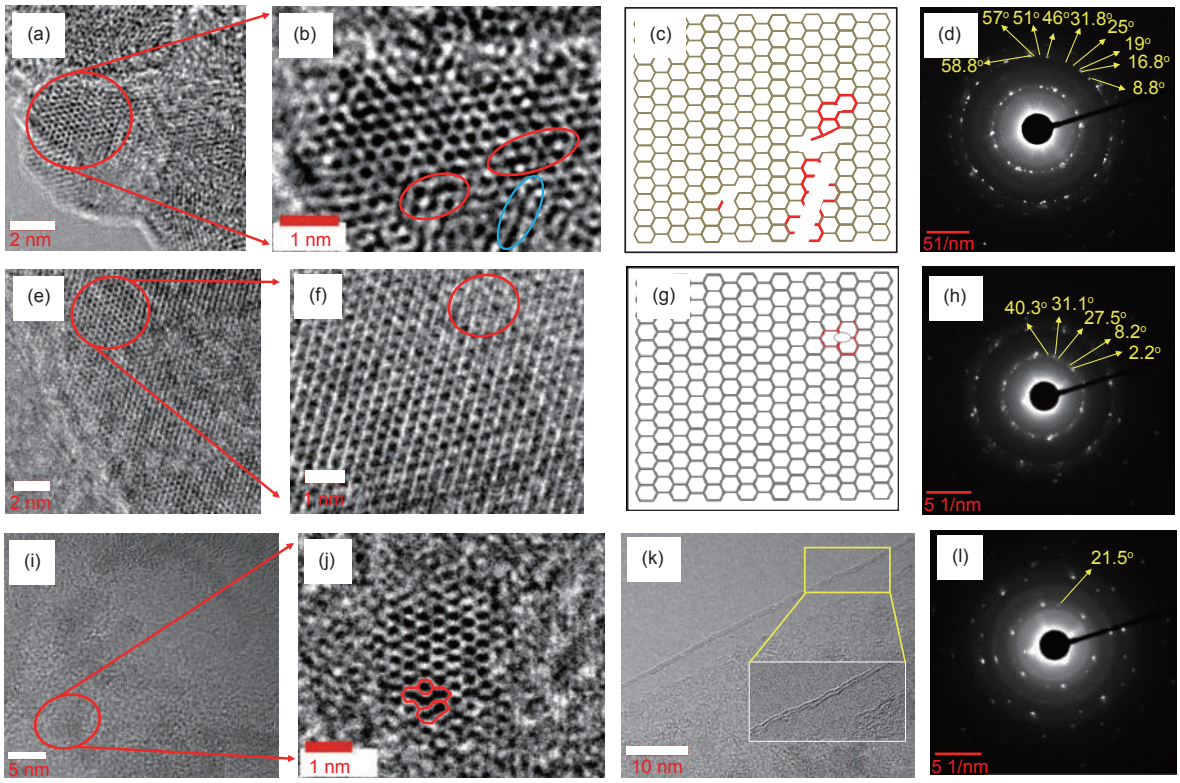

Fig. 5　(a, b) High-resolution TEM images, (c) schematic of graphene lattice with defects, and (d) SAED pattern of Ar-70. (e, f) High-resolution TEM images, (g) schematic of graphene lattice with defects, and (h) SAED pattern of Ar-80. (i, j) High-resolution TEM images, (k) BLG edges, and (l) SAED pattern of Ar-100

j). The inset of Fig. 5(k) shows the high-resolution TEM image of 2 atomic-carbon layers. The SAED pattern in Fig. 5(l) shows the non-Bernal stacked or twisted BLG with a twist angle of 21.5°. The Ar-100 sample also shows some traces of SLG that confirm the proper etching of copper foil with H_2 dilution, shown in Fig. S5(f). As the defects are healing with H_2 dilution, turbostratic factor (F) is approaching pristine SLG (1°). Turbostraticity is calculated with the help of the SAED pattern (Fig. S6) from equation S1, and the results are summarized in Table S1.

The above discussions are also confirmed by X-ray photoelectron spectroscopy (XPS). The C1s result of Ar-100 is found to be similar to those for the pristine BLG (Fig. 6(a)). The sp^2 carbon peak (284.84 eV) is symmetrical with fewer functional groups. Additional spectral peaks were assigned to alcohol (—COH) and ester (O=C—O) at 285-286 and ~ 288 eV. The O1s spectrum in Fig. 6(b) is deconvoluted into 4 major peaks at 529.95, 530.68, 531.62 and 532.87 eV labelled as metal oxides (Me-O_x), O=C, O—C and H_2O, respectively. An additional impurity (SiO_2) appeared due to the oxide formation inside the quartz chamber or from environmental exposure.

XPS results in Fig. 6(c) are interesting and show a trend between carbon, copper and oxygen amount. The sp^2 content in the samples increased from 5% (Ar-70) to 28% (Ar-100), on the other hand copper content got reduced from 77% (Ar-70) to 61% (Ar-100), calculated from equation(S2). The O1s presence is also suppressed at 18% (Ar-70), 14% (Ar-80), and 11% (Ar-100). Fig. 6(d) shows the XPS depth profile of Cu2p of Ar-100. A thin layer of CuO promoted and formed on the top of Cu and Cu_2O[25–26] that can be understood by equation (4):

$$Cu_2O + O \rightarrow 2CuO \qquad (4)$$

Finally, from the above optimizations, SLG is grown by increasing the growth time (25 min) only. A high-quality SLG (I_{2D}/I_G = 4) is obtained (Fig. 7(a)). Fig. 7(b, c) shows high-resolution TEM images of SLG. A single crystalline SAED pattern of SLG is shown in Fig. 7(d) which is further used for the

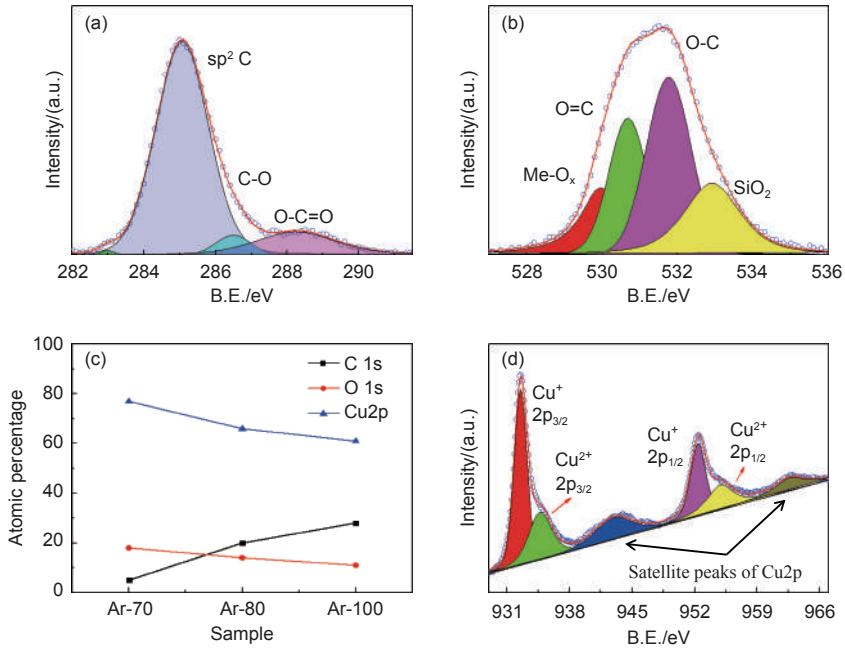

Fig. 6 High-resolution XPS spectra of (a) C1s, (b) O1s of Ar-100 sample, (c) atomic percentage comparison of C1s, O1s, and Cu2p, and (d) spectra of Cu2p

demonstration of flexible and lightweight RTP-CVD-grown graphene for thermal management consumer electronics.

We demonstrated a feasible heat sink installed on a 2TB SSD (NVMe M.2 TCM2-C3) with a transmission rate of 10 Gbps using RTP-CVD-grown graphene (Fig. 8(a)). To generate heat for the temperature measuring method, 40 GB of data were transmitted from the laptop to the 2TB SSD for 3 min before the data flow was stopped. Fig. 8(b) illustrates the measured temperatures of the 2TB SSD after 3 min for the commercial copper, commercial aluminium, Ar-70, Ar-100 and SLG heat sinks, respectively. SLG is advantageous for heat dissipation since it offers a high surface area where heat exchange can take place. The 2TB SSD that was mounted *via* SLG thus had the lowest temperature. SLG is capable of dissipating heat 200 times more quickly than conventional copper heat dissipators. High-temperature stability is achieved by the SLG heat sink's fast dissipation of heat from the

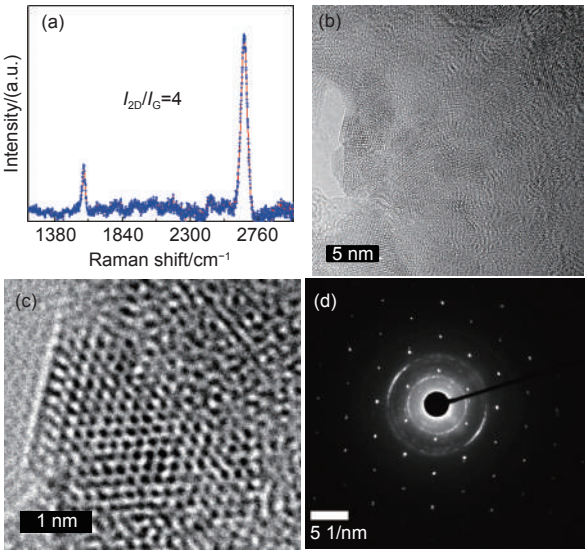

Fig. 7 (a) Raman spectrum, (b, c) high-resolution TEM, and (c) SAED pattern of SLG

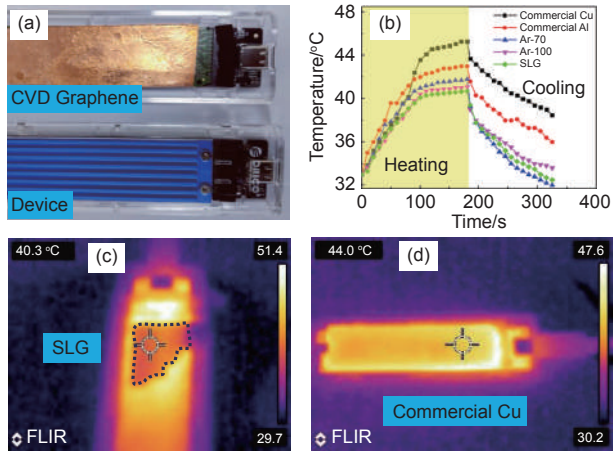

Fig. 8 (a) Photographs of 2 TB SSD (108 (L) mm×34 (w) mm×11.5 (H) mm) with RTP-CVD graphene and commercial aluminium heat sink. (b) Temperature versus time profile of various heat sinks. Demonstration photographs of (c) a thermal IR camera with SLG and (d) commercial copper heat sink

2TB SSD so that it does not build up. The obtained results are compared with published works in Table S2.

4 Conclusions

In this study, RTP-CVD-grown graphene was used to demonstrate heat dissipation with excellent properties. The quality of graphene was optimized and monitored with Raman spectroscopy and high-resolution TEM to get SLG on the copper substrate. High thermal conducting graphene recipes were prepared by diluting H_2 concentration. At a growth temperature of 1 000 °C and growth time of 25 min, respectively, pure SLG was prepared. The RTP-CVD-grown SLG was confirmed to have a good heat dissipation capability owing to its wide surface area. To demonstrate the heat dissipation capability of graphene, a 2TB SSD was used and the temperature was measured by FLIR IR-thermal camera. The SLG mounted on the 2TB SSD exhibited the lowest temperature of 40.7 °C. Compared to commercial copper heat dissipators, the heat spreading capacity of SLG is found to be around 200 times faster. Consumer devices like laptops, tablets and cell phones are anticipated to include RTP-CVD-grown SLG for thermal management.

Conflicts of interest

There are no conflicts to declare.

Acknowledgements

Author thanks Director CSIR-AMPRI, Bhopal for providing the characterization facilities. The authors would also like to acknowledge the CSIR-NET fellowship (31/041(0078)/2019-EMR-I) and the Raman spectrometer (IndiRam CTR-300, Technos Instruments) supported by the NMITLI project. The TEM work was performed at the Analytical HRTEM laboratory, CSIR-AMPRI, Bhopal supported by CSIR under the Facility Creation Project (MLP0110). The XPS analysis was carried out using a SPECS-GmBH surface analyzer, UGC-DAE Consortium for Scientific Research, Indore.

References

[1] Kercher D S, Lee J B, Brand O, et al. Microjet cooling devices for thermal management of electronics[J]. IEEE Transactions on Components, Packaging and Manufacturing Technology, 2003, 26: 359-366.

[2] Molina-Jordá J M. Nano- and micro-/meso-scale engineered magnesium/diamond composites: Novel materials for emerging challenges in thermal management[J]. Acta Materialia, 2015, 96: 101-110.

[3] Li H L, Wu X, Cheng K, et al. One-pot modified “grafting-welding” preparation of graphene/ polyimide carbon films for superior thermal management[J]. New Carbon Materials, 2021, 36: 949-960.

[4] Chen J, Domingue J C, Sears C L. Microbiota dysbiosis in select human cancers: Evidence of association and causality[J]. Seminars in Immunology, 2017, 32: 25-34.

[5] Balandin A A, Ghosh S, Bao W, et al. Superior thermal conductivity of single-layer graphene[J]. Nano Letters, 2008, 8: 902-907.

[6] Li H L, Xiao S N, Yu H L, et al. A review of graphene-based films for heat dissipation[J]. New Carbon Materials, 2021, 36: 897-910.

[7] Dong Z J, Sun B, Zhu H, et al. A review of aligned carbon nanotube arrays and carbon/carbon composites: fabrication, thermal conduction properties and applications in thermal management[J]. New Carbon Materials, 2021, 36: 873-896.

[8] Lindsay L, Broido D A, Mingo N. Flexural phonons and thermal transport in graphene[J]. Physical Review B, 2010, 82: 2-7.

[9] Stankovich S, Dikin D A, Piner R D, et al. Synthesis of graphene-based nanosheets via chemical reduction of exfoliated graphite oxide[J]. Carbon, 2007, 45: 1558-1565.

[10] Kim K S, Zhao Y, Jang H, et al. Large-scale pattern growth of graphene films for stretchable transparent electrodes[J]. Nature, 2009, 457: 706-710.

[11] Seah C M, Chai S P, Mohamed A R. Mechanisms of graphene growth by chemical vapour deposition on transition metals[J]. Carbon, 2014, 70: 1-21.

[12] Zhang L, Hou G, Zhai W, et al. Aluminum/graphene composites with enhanced heat-dissipation properties by in-situ reduction of graphene oxide on aluminum particles[J]. Journal of Alloys and Compounds, 2018, 748: 854-860.

[13] Bin Kim C, Lee J, Cho J, et al. Thermal conductivity enhancement of reduced graphene oxide via chemical defect healing for efficient heat dissipation[J]. Carbon, 2018, 139: 386-392.

[14] Rho H, Jang Y S, Bae H, et al. Fanless, porous graphene-copper composite heat sink for micro devices[J]. Scientific Reports, 2021, 11: 1-7.

[15] Deokar G, Avila J, Razado-Colambo I, et al. Towards high quality CVD graphene growth and transfer[J]. Carbon, 2015, 89: 82-92.

[16] Papon R, Pierlot C, Sharma S, et al. Optimization of CVD parameters for graphene synthesis through design of experiments[J]. Physica Status Solidi (B):Basic Research, 2017, 254: 1-7.

[17] Ferrari A C, Basko D M. Raman spectroscopy as a versatile tool for studying the properties of graphene[J]. Nature Nanotechnology, 2013, 8: 235-246.

[18] Wahab H S, Ali S, Abdul Hussein A, et al. Synthesis and Characterization of Graphene by Raman Spectroscopy[J]. Journal of Materials Sciences and Applications, 2015, 1: 130-135.

[19] Ferrari A C. Raman spectroscopy of graphene and graphite: Disorder, electron-phonon coupling, doping and nonadiabatic effects[J]. Solid State Communication, 2007, 143: 47-57.

[20] Lin Y C, Lu C C, Yeh C H, et al. Graphene annealing: How clean can it be?[J]. Nano Letters, 2012, 12: 414-419.

[21] Vlassiouk I, Smirnov S. Graphene nucleation density on copper: fundamental role of background pressure[J]. The Journal of Physical Chemistry A, 2013, 117: 18919-18926.

[22] Riikonen S, Krasheninnikov A V, Halonen L, et al. The role of stable and mobile carbon adspecies in copper-promoted graphene growth[J]. The Journal of Physical Chemistry C, 2012, 116: 5802-5809.

[23] Muñoz R, Gómez-Aleixandre C. Review of CVD synthesis of graphene[J]. Chemical Vapor Deposition, 2013, 19: 297-322.

[24] Zhang X, Guo X, Sun X, et al. Roles of CuO and Cu_2O in graphene growth on a copper substrate[J]. Applied Surface Science, 2022, 576: 151812.

[25] Sahai A, Goswami N, Kaushik S D, et al. $Cu/Cu_2O/CuO$ nanoparticles: Novel synthesis by exploding wire technique and extensive characterization[J]. Applied Surface Science, 2016, 390: 974-983.

[26] Gan Z H, Yu G Q, Tay B K, et al. Preparation and characterization of copper oxide thin films deposited by filtered cathodic vacuum arc[J]. Journal of Physics D:Applied Physics, 2004, 37: 81-85.